

14,13

## Electron Transport Mechanisms in Polyethylene Terephthalate Membranes

© A.K. Fedotov<sup>1</sup>, S.A. Movchan<sup>2</sup>, P.Yu. Apel<sup>2</sup>, J.A. Fedotova<sup>1</sup>, A.V. Pashkevich<sup>1,3</sup>

<sup>1</sup> Research Institute for Nuclear Problems of Belarusian State University, Belarus

<sup>2</sup> Joint Institute for Nuclear Research, Russia

<sup>3</sup> Belarusian State University, Belarus

E-mail: akf1942@gmail.com

Received Januari 3, 2022

Revised March 1, 2022

Accepted May 14, 2022

This paper describes carrier transport mechanisms in polyethylene terephthalate (PET) films and porous PET-based membranes (PMs) obtained by irradiating pristine PET film with swift heavy ions, with subsequent chemical etching in an alkali (NaOH) solution. The obtained PMs had through nanochannels (pores) with an average diameter of 720–750 nm. We observed that in the temperature range 240–300 K, the current-voltage characteristics  $I(V)$  of the initial Cu|PET|Cu structure obeyed the improved Mott–Gurney law, which is based on the Mark–Helfrich model for a space-charge-limited current (SCLC) mechanism for electron transport. It was found for the first time that creation of nanochannels in PMs resulted in a significant increase in the electric current density (by about three orders of magnitude) while maintaining the SCLC mechanism. The enhanced current density is explained by the formation of a highly conductive layer along the inner surface of the walls of the nanochannel that are covered with carboxyl end groups, which are created by alkaline hydrolysis. According to the model, the surface states formed by these groups enable the drift of additional electrons injected from the copper electrodes under the action of the bias voltage.

**Keywords:** polyethylene terephthalate, electron transport, space-charge-limited current mechanism, Mark–Helfrich injection model.

DOI: 10.21883/PSS.2022.10.54251.269

### 1. Introduction

The fabrication of reliable flexible conductive substrates is still a significant challenge that needs to be overcome for the widespread application and commercialization of wearable electronics [1]. Polyethylene terephthalate (PET) foils are among the most used polymeric materials. PET is stable in acids and organic solvents, biologically inert, and mechanically stable and strong [2–4]. PET continues to attract considerable attention given its good performance parameters in a variety of other applications. In particular, as a result of significant polar bonds between molecular chains, PET films are characterized by lower values of the dielectric constant  $\epsilon$  (no higher than 3.4 [1,3]) compared with, for example, silicon oxide. This feature can be used to create insulating layers in ultra-large-scale integrated circuits to achieve the maximum possible operating speed in electronic devices while reducing their size to a nanometer scale [5]. In addition, PET films exhibit good surface planarization with low values for mechanical stress and high electric breakdown fields [1]. These features underlie the potential application of PET foils as flexible platforms for 2D optoelectronic devices and wearable electronics [6]. Moreover, PET films could serve as suitable substrates for

the formation of various types of hybrid heterostructures using PET in combination with metallic, semiconducting, and other types of two-dimensional layers, including graphene.

Flexible, wearable, and standard electronics can be designed from PET films based on porous membranes (PMs) with artificially grown vertical channels (pores) formed by etching latent tracks with irradiation by swift heavy ions (SHI). The process of track formation and etching in PET has been extensively studied [2,7,8]. A high track-to-bulk etch rate ratio is achievable (when using sensitization with ultraviolet radiation), making it possible to produce a wide range of membranes with various pore diameters. The etching procedure is simple and fast. Alkali solutions (sometimes with additives) are used as etchants to develop latent tracks in polyesters.

To design new devices with controllable performance characteristics using PET PMs as flexible platforms, we need to study changes in the mechanisms for electric conductivity resulting from the formation of pores (nanochannels) in the PET foil. We believe that expected variations in the electric conductivity characteristics of PET membranes are governed not only by their porosity but also by the properties of the internal pore surfaces and interfaces between the metallic electrodes and PM.

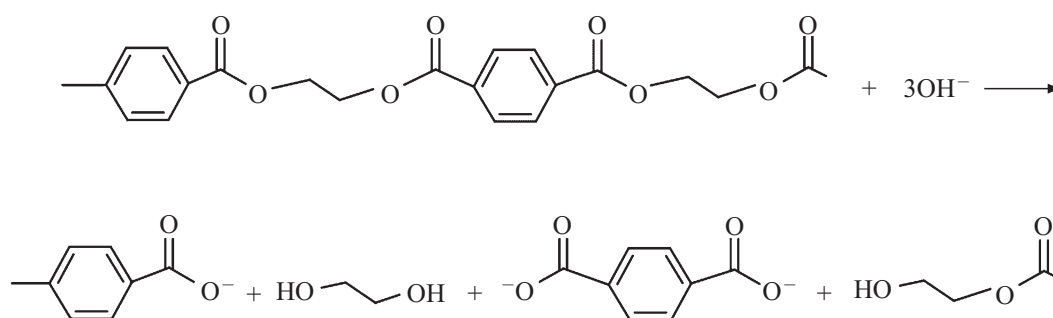


**Figure 1.** Reaction of the alkaline hydrolysis of PET. Carboxyl and hydroxyl groups (leftmost and rightmost, respectively, in the bottom line) are the reaction product localized on the etched surface [14] on the type of metallic contact and physical-chemical state of the metal-PET interface.

There are few works in the literature on the mechanisms for the electrical conductivity of PET films (especially below room temperature) that is associated with the high electrical resistivity of PET. The mechanisms for conduction in PET films have mainly been studied above room temperature, up to the crystallization temperature (of the order of 400 K) for amorphous samples and at higher temperatures for crystalline samples. The results of these studies, presented in papers [9–12], show the activation characteristics of the temperature dependences for electrical conductivity. However, these works give contradictory results for activation energies, which vary from 0.4 to 2.58 eV depending on the type of metallic electrodes. Moreover, there are significant contradictions when explaining the mechanisms for electric transport, which are used to interpret the current-voltage characteristics  $I(V)$ . These contradictions can be attributed to the different relative content of the amorphous and crystalline phases in the PET samples studied, as well as to the different types and quality of electrical contacts used in electrical measurements. In works [11,12] the studied  $I(V)$  characteristics of pristine PET films in the temperature range of 300–400 K were described based on the Schottky injection model. On the other hand, work [10] denies the applicability of this model, leaning towards the validity of the space-charge-limited current (SCLC) model. As shown in a recent study [6], the high resistance of PET samples can be overcome, since it is largely due to the type and quality of the electrodes used (see below); this makes it possible to study the mechanisms for electric transport in a temperature range significantly below room temperature.

This study aims to examine the transformation of charge-carrier transport in PET foils after pore formation by etching latent tracks introduced by SHI irradiation before the deposition of copper electrodes.

## 2. Experimental

Porous PET membranes were produced using a three-stage process: (a) irradiation of the initial PET film with SHI, (b) exposure to ultraviolet (UV) radiation, and

(c) chemical etching. First, PET films with a thickness of 10  $\mu\text{m}$  were irradiated at the U-300 cyclotron facility of Flerov Laboratory of Nuclear Reactions (JINR, Dubna) using a beam of Xe ions with an energy of 1 MeV/nucleon [13]. After appropriate UV exposure, chemical etching took place in an alkali solution (NaOH) [2]. The etching resulted in the formation of cylindrical hollow channels with an average diameter of 720–750 nm, and the film thickness was reduced to 9.3  $\mu\text{m}$ . The alkaline etching of polyester involves a sequence of ester bond cleavages. Fig. 1 shows two repeating units of PET, the alkaline hydrolysis of which yields ethylene glycol, an anion of terephthalic acid, and both carboxyl and hydroxyl groups at the ends of macromolecular chains [2,7,8]. In basic and neutral environments, the carboxyl group exists as a carboxylate. The dangling carboxylate and hydroxyl donor-like end groups (see the upper line in Fig. 1), formed on the inner surfaces of the nanochannels, largely determine the properties of the etched PET membrane.

After the etching of the nanochannels, both sides of a pristine PET film and porous membrane samples were covered with 80-nm thick Cu layers as electrodes using a sputtering method. As shown in previous papers, the electrical properties of pristine PET films are strongly dependent on the type of metallic contact and the physical-chemical state of the metal-PET interface.

Research conducted in [6] showed that among different metals as electrodes (Au, Al, Cu, Ni, Ti, etc.), the Cu layers exhibit the lowest conductivity at the interface between pristine bulk PET and the electrode. According to [6], the quality of the contact between bulk PET and Cu depends on the roughness of the Cu–PET interface, adhesion of Cu onto the surface of the PET film, and the duration of Cu deposition, as well as the cathode sputtering technique used when depositing the Cu layer. It was observed that the resistance of the Cu|PET|Cu structure decreases steadily due to the formation of a continuous network between the Cu nanoparticles in the under-surface layer of the PET with increasing deposition time. The increased occurrence of Cu nanoparticles at the Cu–PET interface eventually results in aggregate connectivity and increased conduction pathway

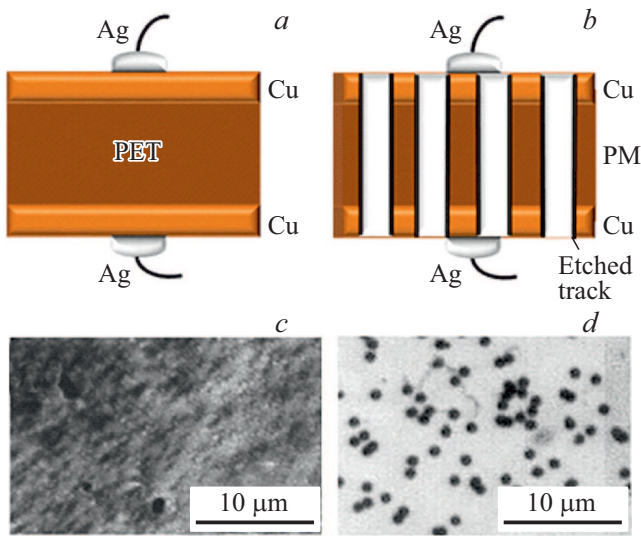


**Figure 2.** Schematic cross-sectional view (*a* and *b*) and optical micrographs (*c* and *d*) of the studied samples: *a* and *c* relate to Cu|PET|Cu, *b* and *d* to Cu|PM|Cu.

formation, improving the overall electrical properties of the Cu|PET|Cu structure [6]. In our experiments, the resistance of the Cu|PET|Cu structure decreased with the increased thickness of the Cu layer from 20 to 180 nm, approaching the lowest values at a thickness greater than 70–80 nm. Thus, in our Cu|PET|Cu structures, we used Cu electrodes about 80 nm thick.

The Cu|PET|Cu structures formed without pores (pristine PET) and with pores are shown in Fig. 2, *a* and *b* schematically and in Fig. 2, *c* and *d* as the upper view of optical images. Additional SEM images of surface and cross section of the Cu|PM|Cu structures are shown in Fig. 3. It follows from the optical microscopy data in Figs. 2, *c* and *d* that the density of pores was approximately 15–17%, and their average diameter was about 720–750 nm. Note also that the presence of nanopores in the PET membrane did

not change after copper electrode deposition, as reflected in Fig. 2, *d*.

The transverse current-voltage characteristics  $I(V)$  were measured using samples  $2 \times 3 \text{ mm}^2$ , as shown schematically in Figs. 2, *a* and *b*. For  $I(V)$  measurements, copper wires 0.1 mm in diameter were attached by silver paste to the Cu layers on both sides of the structure (Figs. 2, *a* and *b*). Then, the wires were soldered with indium to the gold-plated electrical contacts of a special measuring cell. The cell with a soldered sample was connected either to the impedance meter directly or to a cryogenic connector of a measuring probe, the upper part of which was connected to a cryogenic measuring system on the base of a closed-cycle refrigerator. The  $I(V)$  characteristics in the form of  $J(E)$  dependences ( $J$  is current density,  $E$  is electric field intensity) were measured in a temperature range of 240–300 K with electric bias fields of  $E \leq 2 \cdot 10^6 \text{ V/m}$ , applied normally to the surface of structures, by Keithley 6430 power supply with a current meter and Keithley 3485 voltmeter in an automatic mode at a bias voltage sweep rate of 0.1 V/s.

To measure and control the temperature, a Lakeshore 340 controller was used, and this stabilized the temperature with an accuracy of 0.005 K during the sweep of the bias voltage. The temperature of the samples was measured with calibrated LakeShore thermal diodes. Due to the high electrical resistance of the PET film (which reached 100–120 MΩ at room temperature) and the limited input resistance of the Keithley voltmeter 3485 and Agilent LCR meters (no higher than 20 GΩ), the  $J(E)$  curves of the initial PET film could be measured with an accuracy of no worse than 1% only at temperatures above 230 K. At lower temperatures, the resistance of the samples reached values exceeding 1 GΩ, and the results of measurements could not be considered reliable.

To check the value of dielectric permittivity, we also measured the dielectric constant of the Cu|PET|Cu and Cu|PM|Cu structures at room temperature in a frequency range of 1–1000 kHz, using an Agilent-type LCR meter.

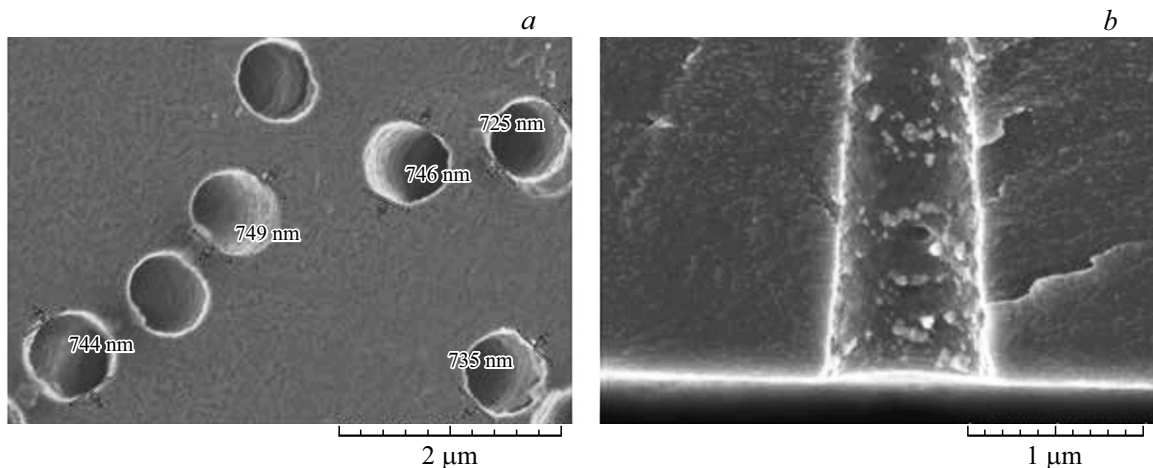


**Figure 3.** SEM image of a surface (*a*) and a cross-section of a single pore (*b*) for the PM.

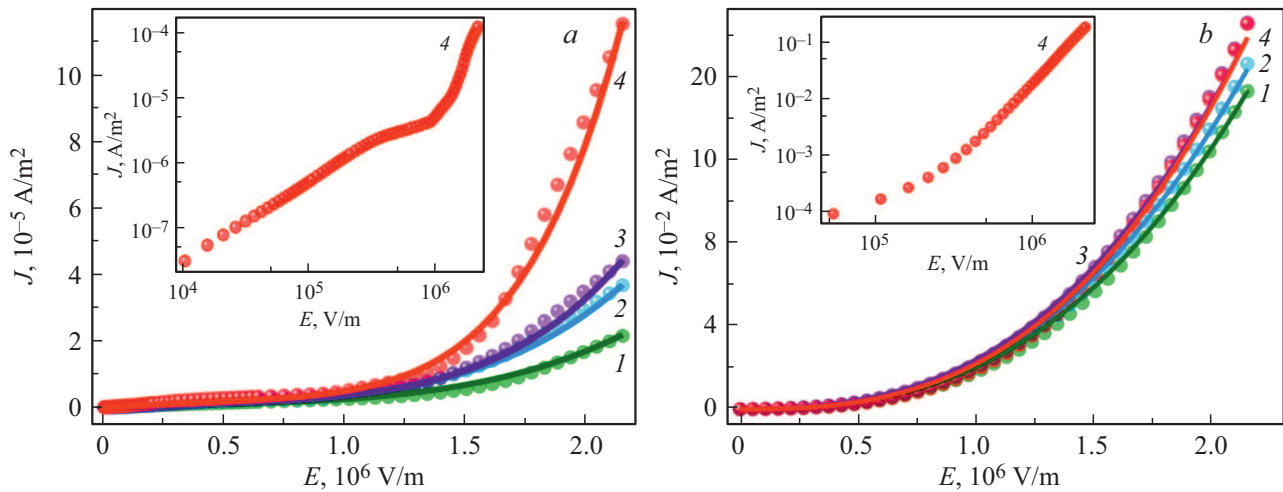


**Figure 4.** Experimental (dots) and calculated (solid lines) dependences of the current density  $J$  on the field strength  $E$  in linear coordinates for samples of the initial PET film (a) and PM (b) at various temperatures  $T$ : 1 — 240, 2 — 260, 3 — 280, 4 — 300 K. The inset shows the  $J(E)$  dependence on a logarithmic scale.

It was found that the frequency dependences of the phase-shift angle  $\theta$  and the specific total impedance  $Z(f)$  of the structures under study indicated their capacitive behavior, allowing us to estimate the dielectric constant without noticeable error using the formula  $\varepsilon = Cd/(\varepsilon_0 S)$ , where  $d$  is the thickness of the polymer film,  $S$  is the area of the capacitor (structure), and  $\varepsilon_0$  is the dielectric constant of vacuum. These measurements show that in the samples of the initial PET film and PM the values of permittivity were about  $\varepsilon \approx 3.6 \pm 0.1$ , which is close to the values given in the reference works [1,3,5].

### 3. Measurement results

The experimental  $J(E)$  dependences observed for the Cu|PET|Cu and Cu|PM|Cu structures are presented in Fig. 4. To understand the mechanisms of electron transport in the studied samples at different temperatures, the  $J(E)$  curves were re-plotted using coordinates corresponding to different models for charge-carrier transport. In particular, we first tested the presence of mechanisms for trap-enhanced tunneling through the polymer layer (Poole–Frenkel model) or the emission of charge carriers from a metal electrode into the polymer (Schottky–Richardson model) [14–17]. According to these models, the rearrangement of the experimental curves  $J(E)$  in the coordinates  $\text{Ln}(J/AT^2)$  vs  $E^{1/2}$  should lead to their linearization in weak electric fields. The slopes of the linear sections allow calculation of the values of the barrier heights  $\varphi_b$ , which are overcome by the charge carriers injected from the metal contact into the pristine PET or PM layer while moving in the polymer bulk. The coordinates of the cutoff segment on the  $J$ -axis allow estimation of the value of the coefficient  $\beta$ , which should be equal to 1 for the Poole–Frenkel mechanism and 2 for the Schottky–Richardson mechanism.

It should be noted that, in our case, the linearization of coordinates  $\text{Ln}(J/AT^2)$  vs  $E^{1/2}$  was achieved in the region of strong fields  $E > (5-10) \cdot 10^5$  V/m. This fact, as well as physically unrealistic values of the coefficient  $\beta$  ( $\ll 1$ ) obtained as a result of linearization, means that the Poole–Frenkel and Schottky–Richardson mechanisms are not suitable for describing  $J(E)$  dependences in the studied structures at the studied temperature range. This finding is consistent with previous work [10] above room temperatures.

The re-plotting of the curves  $J(E)$  in the coordinates  $\text{Ln}(J/E^2)$  vs  $E^{-1}$ , corresponding to the Fowler–Nordheim model [15–18], led to their linearization in weak, but not in strong, electric fields, in line with theory. Moreover, re-plotting gives values of the barrier height (less than  $10^9$  eV) that are physically too low, indicating that the Fowler–Nordheim model is also inappropriate for describing the  $J(E)$  dependences in the studied temperature range, as confirmed in works [9–12].

Understandably, the above models do not describe the  $J(E)$  dependences in the studied samples, since, according to the literature, these mechanisms in high-resistance PET polymer usually manifest themselves at temperatures of about 300–400 K, *i.e.*, no higher than the melting (crystallization) temperatures of PET [4].

Mott and Gurney proposed an ideal injection model that is based on the space-charge-limited current (SCLC) mechanism [16]. Below we present it in a more general form:

$$J(E, T) = en(T) \cdot \mu(T) \cdot E + \varepsilon \varepsilon_0 \mu(T) \frac{E^2}{d}, \quad (1)$$

which is, in fact, the combination of relations (3) and (2) in [19], relations (3.59) and (3.61) in [20], and equations (2.7.2) and (2.7.5) in [21] with the replacement of the bias voltage by the electric field strength. Here,  $d$  is the thickness

of the polymer foil, and  $n$  and  $\mu$  are the concentration and mobility of thermally excited equilibrium free-charge carriers (electrons, in our case), respectively. As follows from the first term in relation (1), the first part of the  $J(E)$  dependence (in weak fields) is described by Ohm's law [15,16,19–21]. According to [19–24], in higher fields a transition from the linear to the quadratic behavior of  $J(E)$  occurs; see the second contribution to relation (1). According to the ideal Mott–Gurney model [16,19–21], this contribution is realized when the concentration of non-equilibrium electrons injected from the metallic electrode under the action of a bias electric field begins to exceed the concentration of equilibrium free-charge carriers generated by the thermal vibrations of the lattice.

The re-plotting of the experimental curves  $J(E)$  in double-logarithmic scale for the studied structures gave two linear sections with different slopes (see the experimental dependences  $\text{Lg}(J)$  vs  $\text{Lg}(E)$  for  $T = 300$  K in the insets to Figs. 4, *a* and *b*). For the samples studied, at  $E < (2–6) \cdot 10^5$  V/m this slope is indeed close to 1, in accordance with the first term of the ideal Mott–Gurney model (1). However, in the area of high electric fields, where  $E > (5–10) \cdot 10^5$  V/m, the exponent at  $E$  (the slope of straight lines) turned out to be much greater than 2, reaching values of the order of 3–4.5 in the initial PET foil, which does not coincide with the exponent in the second term in relation (1) for the ideal SCLC model. After etching, these slopes become close to 2 in the initial Cu|PM|Cu structures (this is probably because the movement of carriers through traps in the PET bulk becomes less efficient owing to the appearance of additional highly conductive channels for current flow).

In this regard, instead of model (1), we used the improved (combined) Mark–Helfrich approach [15,20,21], giving the following relation for the SCLC model:

$$J(E) = en(T) \cdot \mu(T) \cdot E^{m_1} + e\mu(T)N_c \left[ \frac{\varepsilon\varepsilon_0 m_2}{eN_t(m_2 + 1)} \right] \left[ \frac{2m_2 + 1}{m_2 + 1} \right] \frac{E^{m_2}}{d^{2m_2}}, \quad (2)$$

when fitting the  $J(E)$  curves. Relation (2) is the sum of equations (3.94) and (3.95) in reference [20] in the SCLC model. In relation (1), the exponent in the first contribution (at low fields) equals  $m_1 \approx 1$ , but the exponent  $m_2 = (l + 1)$  in the second contribution (at high fields) may significantly exceed 2. In the indicated model (2),  $e$  is the electron charge,  $n$  is the carrier concentration,  $\mu$  is the carrier mobility,  $N_c = (1/2\pi^2)(2m_0kT/\hbar^2)^{3/2}$  is the effective density of delocalized and localized states in the conductance band,  $N_t$  is the concentration of traps in the „tail“ of localized states in the conductive band below the „mobility edge“  $E_c$  (see Fig. 5 and the explanation below), and the exponent  $m_2$  in the high-field contribution of model (2) equals:

$$m_2 = \left( \frac{E_{th}}{kT} \right) + 1. \quad (3)$$

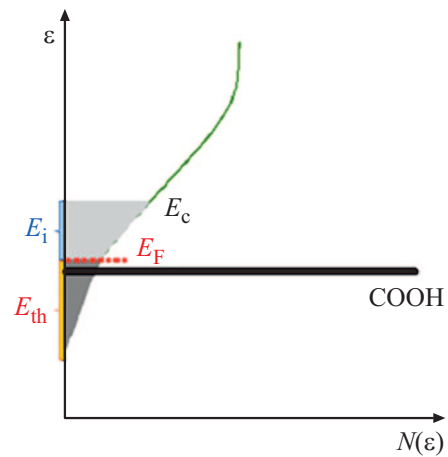


**Figure 5.** A schematic view of the distribution  $N(\varepsilon)$  of delocalized and localized states in the conduction band for the Cu|PM|Cu structure. The white area above „mobility edge“  $E_c$  represents delocalized states. The gray area represents an exponential-like distribution of localized states in the „tail“ below  $E_c$  [20]. In doing so, the light-gray part with  $E_i$ -width corresponds to empty localized states and the light-gray part with  $E_{th}$ -width corresponds to the localized states occupied by electrons. The narrow black strip near the Fermi energy  $E_F$  symbolizes the additional localized states formed by COOH groups on the inner surfaces of the etched pores and which result in extra current in  $I(V)$  in Fig. 4, *b*.

Note that according to [19–21], relation (3) is applicable only for the presence of traps with exponential distribution of the density of the localized state in the „tail“ below the „mobility edge“  $E$  given by the relation:

$$N(\varepsilon) = N_c \exp[(E_c - \varepsilon)/E_{th}]. \quad (4)$$

In this case, according to the improved Mark–Helfrich model (2) [19–21], the concentration of donor-like traps in disordered systems is described by the expression:

$$N_t = \int_{E_c}^{E_v} N(\varepsilon) [(1 - f(\varepsilon))] d\varepsilon \approx [\varepsilon/E_{th}] \exp(-\varepsilon/E_{th}), \quad (5)$$

where  $f(\varepsilon)$  is the function of the occupation of traps per unit of energy  $\varepsilon$  (if the countdown is from the  $E_c$ ). In this case, as shown in [20], the characteristic energy  $E_{th} \equiv k_B T_c$  depends on a certain characteristic temperature, which, being dependent on the position of the temperature-dependent Fermi level, is given in the form of relation (3). In other words, for the exponential distribution of traps by energy in Fig. 5 (below the „mobility edge“  $E_c$ ), the  $m_2$  exponent in model (2) determines the energy width  $E_{th}$  of the „tail“ localized states below  $E_F$ , occupied with electrons. This region of  $N(\varepsilon)$  is represented by the dark-gray color in the schematic view in Fig. 5.

We would like to clarify important points concerning Fig. 5. This figure is the generally accepted image of a band energy scheme for any disordered solid (for example, see

**Table 1.** Parameters for the approximation of  $J(E, T)$  dependences for the Cu|PET|Cu structure in the framework of the improved Mark–Helfrick SCLC model (2)

$T$ , K	$m_1$ ( $E < 10^5$ V/m)	$m_2$ ( $E > 5 \cdot 10^5$ V/m)	$E_{th}$ , meV	$N_c$ , $10^{25} \cdot \text{m}^{-3}$	$n$ , $\text{m}^{-3}$	$\mu$ , $\text{m}^2/\text{V} \cdot \text{s}$	$N_t$ , $\text{m}^{-3}$
240	0.80	3.00	83	2.1	$2.1 \cdot 10^{15}$	$5.03 \cdot 10^{-8}$	$2.45 \cdot 10^{23}$
260	1.10	3.20	94	2.3	$3.0 \cdot 10^{15}$	$1.76 \cdot 10^{-9}$	$4.51 \cdot 10^{22}$
280	1.00	3.5	110	2.6	$6.0 \cdot 10^{15}$	$2.26 \cdot 10^{-9}$	$2.76 \cdot 10^{22}$
300	1.00	4.5	140	2.9	$8.0 \cdot 10^{15}$	$2.51 \cdot 10^{-9}$	$6.50 \cdot 10^{21}$

**Table 2.** Parameters for the approximation of the dependences  $j(E, T)$  for the Cu|PM|Cu structure in the framework of the improved Mark–Helfrick SCLC model (2)

$T$ , K	$m_1$ ( $E < 10^5$ V/m)	$m_2$ ( $E > 5 \cdot 10^5$ V/m)	$E_{th}$ , meV	$N_c$ , $10^{25} \cdot \text{m}^{-3}$	$n$ , $10^{15} \cdot \text{m}^{-3}$	$\mu$ , $\text{m}^2/\text{V} \cdot \text{s}$	$N_t$ , $\text{m}^{-3}$
240	0.99	1.70	56	2.1	$9.0 \cdot 10^{17}$	$1.14 \cdot 10^{-8}$	$2.11 \cdot 10^{23}$
260	1.15	1.70	60	2.3	$1.5 \cdot 10^{18}$	$1.10 \cdot 10^{-9}$	$5.53 \cdot 10^{22}$
280	1.04	1.72	66	2.6	$5.5 \cdot 10^{18}$	$1.50 \cdot 10^{-9}$	$6.21 \cdot 10^{22}$
300	0.96	1.81	73	2.9	$7.5 \cdot 10^{18}$	$2.06 \cdot 10^{-9}$	$5.61 \cdot 10^{21}$

Fig. 5.2 in reference [20]), in which localized states (traps for charge carriers) arise. Disorder in this case manifests itself in the form of the appearance of „tails“ of localized states with exponential energy distribution. The appearance of such states is because the bulk of the PET film is highly disordered (practically amorphous). In addition, the film contains a certain quantity of crystalline particles (usually, in the form of microspherulites [4]), which are randomly distributed in the amorphous PET matrix, and additional trap states also appear at the boundaries; all this together gives rise to the band structure shown in Fig. 5. What is new in this figure is that we add to the conventional PET bulk pattern a narrow strip of additional high-density localized states that symbolizes the formation of COOH groups on the inner surfaces of the etched pores. It is these states, eventually, that provide, in our opinion, the appearance of a highly conductive thin layer, through which an excess (with respect to the PET bulk) flow  $J$  of electrons, injected from metal contacts, moves under the action of an electric field  $E$ .

All the  $I(V)$  characteristics were subject to the fitting procedure using model relations (2)–(5) above, allowing us to estimate important parameters of both sets of samples, such as effective concentration  $n$  and effective electron mobilities  $\mu$  for every temperature and density of trap states  $N_t$  in the „tails“ of the localized states in Fig. 5. The fitting procedure was standard and contained two stages. In the first stage, the experimental curves  $I(V)$  were plotted on a double-logarithmic scale, from which the slopes of the rectilinear segments of the dependences  $\text{Lg}(J) \text{ vs } f[\text{Lg}(E)]$  (see insets in Fig. 4) were used to estimate the initial values of the exponents  $m_1$  and  $m_2$  in the regions of low and high fields, respectively. The estimate of  $m_2$  made it possible to determine the initial values of

the parameter  $E_{th}$  from relation (3), which then allowed the estimation of the initial values of the parameters  $N_t$  and  $N(\varepsilon)$  included in relations (4) and (5). The second stage involved reaching the smallest value of the sum of root-mean-square deviations  $\chi^2$  by all experimental points between the experimental and calculated  $I(V)$ s in each range of temperatures and electric fields by enumerating the values of fitting parameters  $n$ ,  $\mu$ , and  $N_t$  included in relation (2). After finding the minimum possible values of parameter  $\chi^2$  with an appropriate (physically based) combination of fitting parameters, the values of  $m_1$ ,  $m_2$ ,  $E_{th}$ , and  $N_t$  were adjusted according to the same procedure. The fitting procedure was repeated until the root-mean-square deviation reached its minimum value.

The values of various parameters obtained by fitting the  $J(E, T)$  dependences according to model (2) in the temperature range 240–300 K are presented in Tables 1 and 2.

Note that fitting for  $E < 10^5$  V/m shows that  $m_1 \approx 1$  at all temperatures, while for  $E > 5 \cdot 10^5$  V/m the exponent  $m_2$  increases with temperature from 3 to 4.5 for pristine PET foil and from 1.7 to 1.8 for PET membrane (the latter is close to the ideal SCLC model (1) developed by Mott–Gurney [15,19–21]). As can be seen from Tables 1 and 2, the  $N_t$  values are between  $6.5 \cdot 10^{21}$  and  $2.5 \cdot 10^{23} \text{ m}^{-3}$ , while the  $E_{th}$  values increase with temperature from 83 to 140 meV for the initial PET foil and from 56 to 73 meV for the membrane.

The values of electron concentration  $n$  and mobility  $\mu$  extracted from fitting  $J(E, T)$  dependences for the initial PET foil, presented in Table 1, do not contradict model (2) or the data in the literature [19–21] across the range of temperatures and electric fields investigated. However, the values for the concentration of carriers  $n$  in Table 2

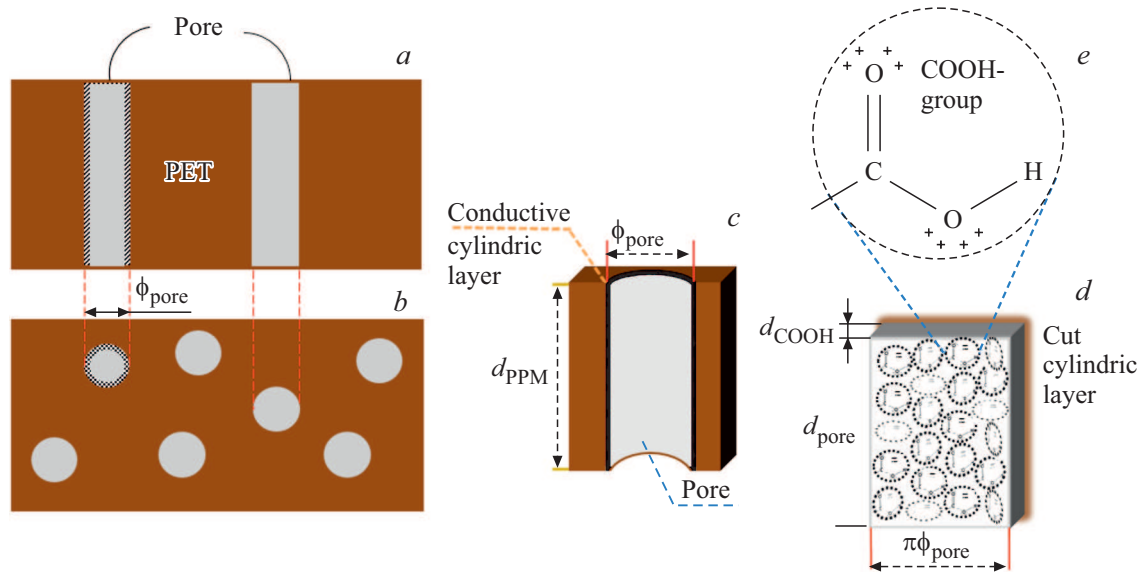


**Figure 6.** Schematic representation of the cross-section (*a*) and top (*b*) views of a porous PET membrane with a thickness of  $d_{\text{PPM}}$ , in which a highly conductive layer (black contour) with a thickness of  $d_{\text{COOH}}$  and diameter  $\phi_{\text{pore}}$  is formed (*c*). The distribution of carboxyl groups (COOH) on an internal surface of the pore (gray ovals) is shown in (*d*). The structure of the COOH group is shown in (*e*).

for the membrane sample are much higher than for the initial PET foil and are matched with a sharp increase in the transverse current density of the PET membrane Cu|PM|Cu in comparison with the initial PET film. For example, at room temperature, the current density  $J$  (and therefore conductivity  $\sigma$ ) increases by almost three orders of magnitude after the etching of pores. In addition, the transverse  $J(E, T)$  characteristics themselves in porous membranes begin to have a weaker dependence on temperature (Fig. 4, *b*) than was observed in the initial Cu|PET|Cu structure (Fig. 4, *a*).

We can attribute the observed excess concentration of electrons migrating along the inner pore surface in the PM sample to the above-mentioned formation of electron traps due to the deposition of carboxyl (COOH) and hydroxyl groups [2,7,8] on the internal surfaces of pores with the use of an alkaline NaOH etchant after irradiation with SHI [3,6]. The observed slight decrease in the mobility of charge carriers  $\mu$  in the PET-based membrane in Table 2 is probably due to their additional scattering on additional traps originating from the presence of COOH and hydroxyl groups. These traps are demonstrated by a sharp, narrow black peak COOH on the density of localized states curve in Fig. 5.

Note that we observed linearization of the  $n(T)$  dependences in Arrhenius scales, which allowed us to estimate activation energies  $E_i$  for these traps, which, according to the band diagram in Fig. 5, fell into localized states in the „tail“ of C-band. Calculations show that in the various types of structures studied, the values of activation energies  $E_i = (E_c - E_F)$  lie in the range 56–103 meV. On the other hand, the  $E_{\text{th}}$  values determined from relation (3) in the combined Mott–Gurney model (2), according to [19–21],

span the energy width of the entire „tail“ of states (below  $E_F$  in Fig. 5) created by traps in the bulk of the PET film. Thus,  $(E_{\text{th}} + E_i)$  provides the full energy width of the localized states (occupied and non-occupied) at different temperatures.

A new feature of the  $J(E, T)$  dependences in the structures studied is that the formation of pores in the PET film leads to the exponent  $m_2$  in the second contribution in model (2) decreasing close to 2, while in the initial Cu|PET|Cu structure  $m_2$  approached 3–4.5. Note also that in the Cu|PM|Cu structure, the value of the exponent  $m_1$  remains close to 1 and the mobility of charge carriers value slightly decreases (Table 2).

Another feature is the large observed deviations between the model dependences  $J(E)$  and the experimental dependences in the range of intermediate values of the electric bias fields in the pristine PET samples. These deviations can be seen, in particular, in the inset to Fig. 4, *a* for the Cu|PM|Cu structure, where room temperature curves  $J(E)$  also are shown in a double-logarithmic scale. In the literature, this fact is most often associated with the transition to the regime of the so-called limiting filling of traps at intermediate fields with an increase in the bias voltage and temperature [24].

Below we present a rough estimate of the thickness  $d_{\text{COOH}}$  of the highly conductive layer formed due to carboxyl (COOH) and/or hydroxyl groups as the main reason for an increase of conductivity of the porous PET membranes, *i.e.*, enhanced increase in the current density when an external bias electric field is applied. We based our estimation on the schematic picture of cross-sectional and top views of the membrane (*a* and *b*) with nanochannels (*a* and *c*) as well as trapping carboxyl groups

( $d$  and  $e$ ) shown in Fig. 6. Note that, according to the literature [25,26], the COOH groups are flat and have a shape close to a trapezoid (Fig. 6,  $e$ ).

The approach described allows us to estimate the effective thickness  $d_{\text{COOH}}$  of the highly conductive layer resulting from the formation of COOH groups on the internal surfaces of pores. We conducted the assessment by comparing the equilibrium conductivities of the Cu|PET|Cu and Cu|PM|Cu structures, which were based on the values of the average concentration  $n$  and mobility  $\mu$  of charge carriers in the PET films in Tables 1 and 2 obtained from the fitting procedure.

From the results of measurements of the  $I(V)$  characteristic in Fig. 4, it follows that the ratio of the conductivities of these two structures (for example, at room temperature and in the maximum electric bias field) is:

$$(\sigma_{\text{Cu|PM|Cu}}/\sigma_{\text{Cu|PET|Cu}}) \approx 1000. \quad (6)$$

Furthermore, we can determine that:

$$\begin{aligned} (\sigma_{\text{Cu|PM|Cu}}/\sigma_{\text{Cu|PET|Cu}}) &\approx [(e n_{\text{PM}} \mu_{\text{PM}})/(e n_{\text{PET}} \mu_{\text{PET}})] \\ &\approx (n_{\text{PM}}/n_{\text{PET}}). \end{aligned} \quad (7)$$

The results of relation (7) mean that the ratio of the conductivities of the initial PET film to the highly conductive layers in the PM is determined mainly by the ratio of the concentrations of charge carriers (electrons) injected into them since the mobilities of the latter ( $\mu_{\text{PET}}$  and  $\mu_{\text{PM}}$ ) in practice do not change.

At the same time, the following relationship can be obtained for the measured current densities flowing through the PET film and all the highly conductive layers formed from COOH groups on the inner surface of the pores in the membrane:

$$\begin{aligned} (\sigma_{\text{PET}}/\sigma_{\text{PM}}) &= (J_{\text{PET}}/J_{\text{PM}}) = (d_{\text{PET}}/S_{\text{PET}})(d_{\text{COOH}}/S_{\text{PET}}) \\ &= d_{\text{PET}}/d_{\text{COOH}}. \end{aligned} \quad (8)$$

Hence, it follows that the thickness of the highly conductive layer formed by COOH groups on the inner surface of the pores in the membrane cannot be higher than:

$$\begin{aligned} d_{\text{COOH}} &= d_{\text{PET}} / \left( \frac{\sigma_{\text{PET}}}{\sigma_{\text{PM}}} \right) \approx d_{\text{PET}}/1000 \\ &\approx 9 \cdot 10^{-6} / 1000 \text{ m} \approx 9 \text{ nm}. \end{aligned} \quad (9)$$

This thickness should be significantly lower, since, in relation (9), the effective current density obtained from the experiments is used, and this is significantly underestimated in comparison with the real current density in the system of highly conductive channels inside the PM. In addition, this estimate does not consider the scatter of pores by diameter or the non-cylindrical shape and non-flatness of real pores (roughness of pore walls in Fig. 3,  $b$ ) when covered with COOH groups. Nevertheless, even without considering these circumstances, the estimated thickness of the conductive layer (9) in the porous PET membrane looks quite plausible as the upper limit of possible values of  $d_{\text{COOH}}$ .

## 4. Conclusion

Experimental and model studies of the  $I(V)$  characteristics of a pristine Cu|PET|Cu structure and porous PET-based membranes (structure Cu|PM|Cu) with nanochannels (pores) of 720–750 nm average diameter were carried out in the temperature range  $T = 240\text{--}300$  K. It has been shown that the room temperature dielectric constant of the structures studied is about  $\epsilon \approx 3.6 \pm 0.1$ , which is close to the data in the literature. We observed that the  $I(V)$  characteristics of the pristine PET foils at temperatures below room temperature are satisfactorily described based on the space-charge-limited current model improved by Mark–Helfrich. The use of this model for the temperature range 240–300 K allowed us to estimate the concentrations and mobilities of electrons in pristine PET, which are (i) thermally excited from traps with exponential distribution by energy in the PET bulk and Cu–PET interface, and (ii) injected into PET film from copper electrodes due to the impact of the bias electric field. In addition, it was found experimentally for the first time that the etching of pores in PET films leads to a significantly stronger (by a factor of about 1000) increase in the electric current through the film than would be due to a simple decrease in the sample area with etching of pores (in the latter case, this would amount to only 15–20%). It has been shown that this effect is a consequence of the formation of COOH groups on the inner surface of the etched pores.

## Acknowledgments

Authors thank M.A. Kuvaitseva, O.L. Orelovich, and N.E. Lizunov for preparation and SEM measurements of samples, and Dr I. Svito for measurements of current-voltage characteristics.

## Conflicts of interests

The authors declare that they have no conflict of interest.

## References

- [1] S.M. Haque, J.A.A. Rey, A.A. Masúd, Y. Umar, R. Albarracin. Ch. 3 „Properties and Applications of Polymer Dielectrics“ in „Properties and Applications of Polymer Dielectrics“ / Ed. Boxue Du. Intech Open (2017). <https://www.intechopen.com/chapters/52876>
- [2] P. Apel. Rad. Measurements **34**, 1–6, 559 (2001).
- [3] M. Kechadi, L. Chaal, V. Vivier, B. Tribollet, J. Gamby. Phys. Chem. Chem. Phys. **18**, 30, 20583 (2016).
- [4] Z. Chen. The Crystallization of Poly(ethyleneterephthalate) Studied by Thermal Analysis and FTIR Spectroscopy. PhD thesis, University of Birmingham (2012). <https://etheses.bham.ac.uk/id/eprint/4251/1/Chen13PhD.pdf>
- [5] W. Volksen, R.D. Miller, G. Dubois. Chem. Rev. **110**, 1, 56 (2010).
- [6] A. Atta, E. Abdeltwab, A. Bek. Research Square (2021). 22 p. DOI: <https://doi.org/10.21203/rs.3.rs-220271/v1>

- [7] H.B. Lück. Nucl. Instruments. Methods **213**, 2–3, 507 (1983).
- [8] S.P. Tretyakova, P.Yu. Apel, L.V. Jolos, T.I. Mamonova, V.V. Shirikova. Proceed. 10th Int. Conf., 283 (1980).
- [9] L.E. Amborski. J. Polymer Sci. **62**, 331 (1962).
- [10] D.M. Taylor, T.J. Lewis. J. Phys. D **4**, 9, 1346 (1971).
- [11] J. Ho, T.R. Jow. IEEE Int. Power Modulator. High Voltage Conf. (IPMHVC), 399 (2012).
- [12] N. Belkahla, N. Saidi-Amroun, M. Saidi, M. Benaissa. Int. J. Polymer Analysis. Characterization **18**, 1, 15 (2013).
- [13] G.N. Flerov, P.Yu. Apel, A.Yu. Didyk, V.I. Kuznetsov, R.Ts. Oganessian. Atomic Energy **67**, 4, 274 (1989).
- [14] P. Apel. Track-etching. In: E.M.V. Hoek and V.V. Tarabara (Eds). Encyclopedia of Membrane Science and Technology. John Wiley and Sons, Inc. (2013). P. 1–25.
- [15] P. Mark, W. Helfrich. J. Appl. Phys. **33**, 1, 205 (1962).
- [16] N.F. Mott, R.W. Gurney. Electronic Processes in Ionic Crystals. Oxford University Press, N.Y. (1940). 209 p.
- [17] S.M. Sze, K.K. Ng. Physics of Semiconductor Devices, 3rd ed. Wiley-Interscience (2006).
- [18] M.A. Lampert, P. Mark. Current Injection in Solids. Academic Press (1970). 351 p.
- [19] J.A. Röhr and R.C.I. MacKenzie. Journal of Applied Physics **128**, 165701 (2020). <https://doi.org/10.1063/5.0024737>
- [20] J.A. Röhr. Measurements and Modelling of Space-Charge-Limited, PhD thesis. Imperial College, London (2018). 248 p.
- [21] A. Sim. Unified Model of Charge Transport in Insulating Polymeric Materials. PhD thesis. Utah State University (2013). 269 p.
- [22] D.R. Lamb. Electrical Conduction Mechanisms in Thin Insulating Films. Methuen and Co., Ltd. (1967).
- [23] P.W. May, S. Höhn, W.N. Wang, N.A. Fox. Appl. Phys. Lett. **72**, 17, 2182 (1998).
- [24] A. Rose. Phys. Rev. **97**, 6, 1538 (1955).
- [25] V.K. Il'yasov, A.N. Lachinov, A.V. Moshelev, A.F. Ponomarev. Phys. Solid State **50**, 3, 568 (2008).
- [26] [https://chem.libretexts.org/Courses/Athabasca\\_university/Chemistry\\_360%3A\\_Organic\\_Chemistry\\_II/Chapter\\_20%3A\\_Carboxylic\\_Acids\\_and\\_Nitriles/20.02\\_Structure\\_and\\_Properties\\_of\\_Carboxylic\\_Acids](https://chem.libretexts.org/Courses/Athabasca_university/Chemistry_360%3A_Organic_Chemistry_II/Chapter_20%3A_Carboxylic_Acids_and_Nitriles/20.02_Structure_and_Properties_of_Carboxylic_Acids)
- [27] C.W. Dence. In: C.W. Dence, S.Y. Lin (Eds). Methods in Lignin Chemistry. Springer (1992). 458 p.